Full-Wave, Finite Element Analysis of Irregular Microstrip Discontinuities

ROBERT W. JACKSON, SENIOR MEMBER, IEEE

Abstract—**Finite element expansion currents are used to formulate a full-wave analysis of microstrip discontinuities. A rigorous analysis of fairly irregular structures is possible, including radiation and surface wave effects as well as coupling between closely spaced junctions. The step, stub, and bent-stub discontinuities are analyzed using this technique. Measurements are presented which verify stub calculations.**

I. INTRODUCTION

IN THE PAST several years, designers of microwave and millimeter-wave integrated circuits have come to depend heavily on computer-aided techniques to reduce design time and improve performance. Most CAD modeling of passive circuits centers on the microstrip circuit medium and includes models of microstrip bends, steps, tees, and other discontinuities [1], [2]. In early integrated circuit designs, these models were used with some success. In recent years, however, increases in operating frequency and higher performance requirements have made some of the earlier models (based on a quasi-static assumption) insufficiently accurate. Fully electromagnetic models are now often required in order to include effects such as dispersion, radiation, and coupling. In addition to higher frequency requirements, smaller, more densely packed circuits are being designed in order to reduce cost. This further increases coupling and makes it awkward to use many of the standard junctions. As a result, irregularly shaped junctions may be necessary to reduce crowding, and modeling of these junctions becomes important. This paper presents a technique for calculating rigorously, at high frequencies, the characteristics of somewhat irregular microstrip junctions.

A number of full-wave techniques have been published for the analysis of such simpler microstrip discontinuities as the open end [3]–[6] and step [7]. Both [5] and [6] used finite element currents (piecewise sinusoids) to model the open-end and gap discontinuities on an open substrate, but in the former case, finite elements were used only in an area local to the discontinuity and precomputed sinusoids were used elsewhere. In [3], [4], and [7], the authors also used precomputed sinusoids but modeled the discontinuity locally with entire domain currents. Some of these junctions may also be analyzed using the full-wave techniques which have been applied to finline junctions [8], [9].

For more complicated or irregular junctions, most analyses use some type of simplifying assumption, such as a quasi-static approximation [10], [11] or a magnetic wall approximation [12]. Exceptions include the use of finite element currents to model irregularly shaped microstrip resonators in a closed cavity [13] and irregularly shaped antennas [14], [15]. The method of lines has also been used to discretize the currents on irregularly shaped microstrip structures in an enclosure [16]. In that reference and in recent work by Rautio and Harrington [17], the entire modeled structures are discretized. The former de-embeds discontinuity parameters from a set of resonator calculations or periodic line calculations. The latter work uses a magnetic source current on the enclosure wall to excite an input microstrip line. The resulting current at that point is used to calculate an admittance which includes both the excitation effects and the discontinuity effects. A de-embedding must then take place.

A formulation is presented here which models microstrip junctions on an open substrate using finite element expansion currents (rooftop functions) and sinusoidal precomputed expansion currents for input and output microstrip lines. In contrast to [16] and [17], only the junction itself is modeled with a fine mesh of finite element currents. This setup allows the finite element resolution to be adjusted to the junction without using a very large number of elements to model the slowly varying input and output currents. A substantial improvement in accuracy and numerical efficiency can be achieved. Also, the junction scattering parameters are determined directly from the amplitudes of the reflected and transmitted sinusoids, and no adjustment for source effects is necessary. When resonator methods [7], [13], [16] are used to determine two-port discontinuity parameters, two or more resonators must be analyzed. This is not necessary when the technique presented in this paper is used. Whereas [5] and [6] use only x-directed currents and subdivide along the x direction, this formulation uses both x- and y-directed currents and subdivides along both directions. This subdivision makes it easier to analyze irregular structures than

Manuscript received November 6, 1987; revised June 20, 1988. This work was supported in part by the Air Force Office of Scientific Research under Contract F49620-82-C-0035.

The author is with the Department of Electrical and Computer Engineering, University of Massachusetts, Amherst, MA 01003.

IEEE Log Number 8824250.

0018-9480/89/0100-0081$01.00 ©1989 IEEE

the methods described in [3]–[7]. Jansen and Wertgen [18] have developed a similar formulation except that the entire structure (sources, feedlines, and discontinuities) is enclosed in a conducting box.

In this analysis, neither cover plate nor sidewalls are assumed to be present [20] and therefore radiation and surface wave losses can occur. The measurements and calculations presented show the effects that these losses can have on the behavior of a common microstrip structure. Changing the analysis to include a cover plate is very easily accomplished. In that case, radiative losses would be due to the excitation of parallel-plate modes [19] instead of surface wave and space wave radiation. Similar effects should occur for discontinuities in an electrically large lossy box.

It should be noted that not including sidewalls is, in most cases, a reasonable assumption, since substrate thicknesses and junction sizes are typically very small compared to the junction's distance from a sidewall. Sidewalls may become important if the operating frequency is near a resonant frequency of the enclosure. A practical circuit is not operated near these frequencies in a high-Q enclosure, since all parts of the circuit will couple to each other through the resonant mode. If operation is required near such a frequency, absorbing material is added to the box (along the cover, for example) in order to damp the resonance. This again causes the wall effect to be small, since a parallel-plate wave traveling out from a discontinuity is substantially damped by the time it reaches a sidewall, is reflected, and returns to the discontinuity. Not including sidewalls in this analysis also generates some very useful redundancies in the numerical calculations.

In what follows, the moment method formulation is discussed very briefly, followed by a more detailed description of the expansion mode setup, along with some of the useful symmetries. Next, results are presented for the step, stub, and bent stub. Three sets of measured data are compared to calculated results for the stubs. Calculations of radiation loss of a quarter-wave stub are compared to measurements. And finally, the effect of coupling between closely spaced discontinuities is demonstrated via the bent-stub configuration.

II. Theory

The generic configuration which will be analyzed is presented in Fig. 1. A grounded dielectric slab is shown which extends to $\pm$ infinity in the x and y directions. No cover plate is assumed, although adding one would be a minor modification. Finite element currents, x- and y-directed, are located in the cross-hatched region and are excited by precomputed incident, reflected, and transmitted sinusoidal currents which overlap the finite element region. Although the configuration as shown assumes $\hat{x}$ propagation on the input/output lines, $\hat{y}$ propagating sinusoids could be added (i.e., for a 90° corner). Also, the sinusoidal input/output lines are shown to be centered around $y = 0$, but they can be offset in the transverse direction if desired. The junction which is to be analyzed is

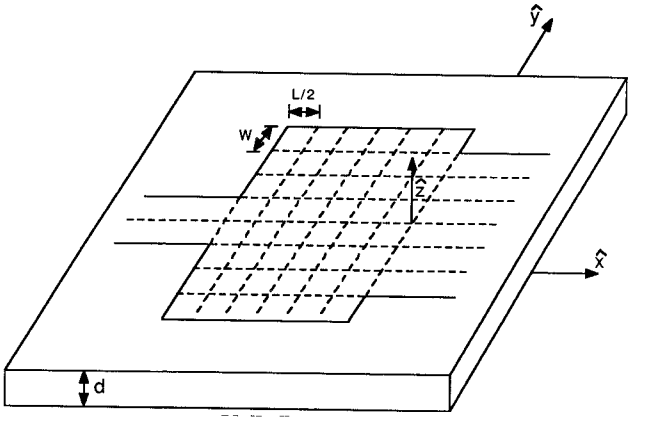

Fig. 1. Arrangement of finite element currents and input/output currents on a grounded dielectric slab. Specific discontinuities form a subset of these currents.

carved out of the finite element region, and this makes it possible to analyze many types of junctions. Examples include open ends, stubs, steps, asymmetric steps, corners, and others. The most significant limitation is that the junction must conform to certain discrete sizes.

A. Moment Method Formulation

Since the method of moments is well known, it is only discussed briefly in order to set the notation and to note some salient points. The formulation, similar to [5], begins by determining the x and y components of the electric field on the surface ($z = d$) of the grounded dielectric slab due to a surface current $\vec{J}$ on the same surface,

$$\vec{E}(x,y) = \frac{1}{(2\pi)^2} \int_{-\infty}^{\infty} \vec{\bar{Q}}(k_x,k_y) \cdot \vec{J}(k_x,k_y) e^{jk_x x} e^{jk_y y}\, dk_x\, dk_y \quad (1)$$

where $\vec{E}(x, y)$ is the two-component surface field, $\vec{J}(k_x, k_y)$ is the Fourier transform of the surface current, and $\vec{\bar{Q}}(k_x, k_y)$ is the Fourier transform of the Green's function for a current element located at the origin (see Appendix I). The current is expanded as follows.

$$\vec{J} = \sum_{j=1}^{NM} A_j \vec{J}_j^e + R\vec{J}^R + T\vec{J}^T + \vec{J}^I \quad (2)$$

where $\vec{J}^R, \vec{J}^T, \vec{J}^I$ are known reflected, transmitted, and incident currents, and the $\vec{J}_j^e$ are rooftop expansion currents, some of which are x-directed and some y-directed. NM is the total number of finite elements, and A_j, R, T are complex coefficients which are to be determined. Weighted averages of the tangential electric field on the microstrip surface are set to zero according to the expression

$$-\int_{-\infty}^{\infty}\int \vec{W}_i(x,y)\cdot\vec{E}(x,y)\,dx\,dy = 0, \quad i = 1,2,3,\cdots,NM+2 \quad (3)$$

where $\vec{W}_i$ are the weighting functions which, except for

two, are the same as the finite element expansion currents. The procedure is therefore almost Galerkin. The resulting matrix has the form

$$\begin{bmatrix} \vec{\vec{Z}} & \vec{\vec{Z}}_{xy} & \vec{Z}_{xR} & \vec{Z}_{xT} \\ \vec{\vec{Z}}_{yx} & \vec{\vec{Z}}_{yy} & \vec{Z}_{yR} & \vec{Z}_{yT} \\ (\vec{Z}_{W1x})^t & (\vec{Z}_{W1y})^t & Z_{W1R} & Z_{W1T} \\ (\vec{Z}_{W2x})^t & (\vec{Z}_{W2y})^t & Z_{W2R} & Z_{W2T} \end{bmatrix} \begin{bmatrix} \vdots \\ A_j \\ \vdots \\ R \\ T \end{bmatrix} = - \begin{bmatrix} \vec{Z}_{xI} \\ \vec{Z}_{yI} \\ Z_{W1I} \\ Z_{W2I} \end{bmatrix} \tag{4}$$

where each impedance term has a form which is similar to, for example,

$$\left(\vec{\vec{Z}}_{xy}\right)_{i,j} = \frac{-1}{(2\pi)^2} \iint_{-\infty}^{\infty} W_i^x(k_x, k_y)^* Q_{xy}(k_x, k_y) \cdot J_j^y(k_x, k_y)\, dk_x\, dk_y. \tag{5}$$

The impedance elements shown in (4) will be described more completely in the next section, but all are a result of a double spectral integration which is performed numerically. This integration includes a careful evaluation of the poles which occur in $Q_{ij}(k_x, k_y)$ [21]. These poles (in practical cases, only one) correspond to surface waves (with no cover) or parallel-plate waves (with cover). In the former case, radiation effects are also included.

After the impedances have been computed, (4) is solved to determine the transmission and reflection coefficients.

Two types of expansion functions and two types of weighting functions are used in this analysis. Rooftop functions are used for expansion and weighting in the junction area, while precomputed sinusoidal currents model the incident, reflected, and transmitted waves which extend away from the junction. Two additional weighting functions are necessary; these will be discussed later.

B. Finite Element Currents

The finite element currents are described by

$$J_j^x(x, y) = t\left([x - x_j]/L\right) \cdot s\left([y - y_j]/W\right) \tag{6a}$$

$$J_j^y(x, y) = s\left(2[x - \bar{x}_j]/L\right) \cdot t\left([y - \bar{y}_j]/2W\right) \tag{6b}$$

where

$$t(u) = \begin{cases} 1 - 2|u|, & |u| < 0.5 \\ 0, & \text{otherwise} \end{cases}$$

$$s(u) = \begin{cases} 1, & |u| < 0.5 \\ 0, & \text{otherwise.} \end{cases}$$

Referring to Fig. 1, the x-directed currents are centered on the $x =$ constant dashed lines at points midway between the $y =$ constant dashed lines, while the y-directed currents are centered on the $y =$ constant dashed lines at points midway between the $x =$ constant dashed lines. The x-directed currents overlap each other in the x direction but not in the y direction, and the reverse is true for the y-directed currents. The same approach was used in [17] except that, in the present formulation, the impedances formed between a weighting current and an expansion current depend only on the position vector separating the two. This would not be true if sidewalls were present (as in [17] and [18]), since the location of the currents with respect to the wall also has an effect when the wall is nearby. The symmetries generated by not having walls plus the symmetries generated by reciprocity make it necessary to calculate only the first row or column of $\vec{\vec{Z}}_{xx}$, $\vec{\vec{Z}}_{xy}$ and $\vec{\vec{Z}}_{yy}$. All the other elements of those matrices and the matrix $\vec{\vec{Z}}_{yx}$ can be determined from them.

C. Sinusoidal Expansion Functions

Ideally the incident, reflected, and transmitted currents would have the form

$$\vec{J}^I = \left[g_x^-(y)\hat{x} + jg_y^-(y)\hat{y}\right]\left[\cos(\beta^- x) - j\sin(\beta^- x)\right] \tag{7a}$$

$$\vec{J}^R = \left[g_x^-(y)\hat{x} - jg_y^-(y)\hat{y}\right]\left[\cos(\beta^- x) + j\sin(\beta^- x)\right] \tag{7b}$$

$$\vec{J}^T = \left[g_x^+(y)\hat{x} + jg_y^+(y)\hat{y}\right]\left[\cos(\beta^+ x) - j\sin(\beta^+ x)\right] \tag{7c}$$

where $\vec{J}^I$ and $\vec{J}^R$ are zero for $x > 0$, and $\vec{J}^T$ is zero for $x < 0$. The functions g_x^- and g_y^- are the transverse variations of the x- and y-directed currents for $x < 0$, and g_x^+ and g_y^+ are the transverse variations for $x > 0$. As discussed in [5], truncating the cosine portion of the x-directed currents at $x = 0$ causes a longitudinal current discontinuity, and numerical difficulties result. Instead, the cosines in (7) are truncated one-quarter guide wavelength from a zero of the sine. The functions then extend away from the junction an integral number of half wavelengths before again terminating. The resulting expansion functions are

$$\vec{J}^I(x, y) = \left[g_{xs}^-(y)\hat{x} + jg_{ys}^-(y)\hat{y}\right] \cdot \left[f^-(\beta^- x + \pi/2) - jf^-(\beta^- x)\right] \tag{8a}$$

$$\vec{J}^R(x, y) = \left[g_{xs}^-(y)\hat{x} - jg_{ys}^-(y)\hat{y}\right] \cdot \left[f^-(\beta^- x + \pi/2) + jf^-(\beta^- x)\right] \tag{8b}$$

$$\vec{J}^T(x, y) = \left[g_{xs}^+(y)\hat{x} + jg_{ys}^+(y)\hat{y}\right] \cdot \left[f^+(\beta^+ x + \pi/2) - jf^+(\beta^+ x)\right] \tag{8c}$$

where

$$f^-(x) = \begin{cases} \sin x, & -n\pi < x < 0 \\ 0, & \text{otherwise.} \end{cases}$$

$$f^+(x) = -f^-(-x).$$

The functions $g_{xs}^-, g_{xs}^+, g_{ys}^-, g_{ys}^+$ model $g_x^-, g_x^+, g_y^-, g_y^+$ and are sums of the functions $s([y - y_j]/W)$ and $t([y - y_j]/2W)$, which were described previously. The exact form of these summed functions and the propagation constants β^- and β^+ are computed before beginning the impedance calculation in (4). This precomputation is fast compared to the discontinuity calculation and is described in Appen-

dix II. Note also that the functions in (8) are normally shifted so as to terminate in the middle of the finite element grid instead of at $x=0$ as described above.

The impedance vectors $\vec{Z}_{xI}$, $\vec{Z}_{xR}$, $\vec{Z}_{xT}$, $\vec{Z}_{yI}$, $\vec{Z}_{yR}$, and $\vec{Z}_{yT}$ are formed by taking the inner product of either W_i^x or W_i^y with one of the currents $\vec{J}^I$, $\vec{J}^R$, or $\vec{J}^T$. For example,

$$\left(\vec{Z}_{yR}\right)_i = \frac{-1}{(2\pi)^2} \iint_{-\infty}^{\infty} (W_i^y)^* \left(Q_{yx} J_x^R + Q_{yy} J_y^R\right) dk_x\, dk_y$$

forms the ith component of the vector $\vec{Z}_{yR}$. (It is understood that W_i^y, J_x^R, J_y^R are the Fourier transforms of the spatial functions described by (6) and (8).)

To determine the dimensions of the impedance matrix in (4), we note that there are $NM_x \cdot NM_y$ x-directed finite element currents, $NM_x \cdot (NM_y - 1)$ y-directed finite element currents, plus the $\vec{J}^R$ and $\vec{J}^T$ currents. So far, we have only tested with finite element functions which total $NM_x \cdot NM_y + NM_x(NM_y - 1)$. As in [4] and [5], two more testing functions are necessary, and these are chosen to be

$$\vec{W}_1(x, y) = t(x) g_{xs}^+(y) \hat{x} \tag{9a}$$

$$\vec{W}_2(x, y) = t(x - x_0) g_{xs}^-(y) \hat{x} \tag{9b}$$

and $x_0 = -(NM_x + 1)L/2$. So these testing functions straddle the lines separating the finite element region and the purely sinusoidal regions (see Fig. 1) and have a y dependence which corresponds to the input and output waveforms. The bottom two rows of (4) obviously result from forming the inner product of these two weighting functions and the various expansion functions.

D. Numerical Considerations

As mentioned previously, because each finite element has the same size and form, and because each mutual impedance depends only on the vector difference between the locations of the two currents involved, many useful redundancies occur. So only the top row of elements in, for example, $\vec{\vec{Z}}_{xx}$ needs to be calculated, and the remaining terms can be determined from them. In addition, due to the shifting property of Fourier transforms, the integrands in each of the impedance elements of the top row differ only by product factors such as $\exp(-jk_xL/2)$ and/or $\exp(-jk_yW)$. Likewise for the other submatrices. Therefore, at each integration point in (k_x, k_y) the integrands of all the necessary impedances within a submatrix differ from their neighbors by one multiplication, and evaluation of the integrand proceeds quickly.

The overall setup of the software is such that *all* the currents in the grid shown in Fig. 1 are assumed to be present initially. Using the various symmetries, the impedance matrix in (4) is computed. Then, at the end of the routine, various rows and columns are deleted so as to form a specific junction out of the general gridwork in the figure. This makes it relatively easy to change the program from analysis of one type of discontinuity to analysis of another. Of course, initially one must choose the size of the input port and the size of the output port and determine the location of these ports in terms of offset and overlap within the finite element region. Several finite current elements are included on the input and output lines in the vicinity of a junction (see Fig. 3 inset) in order to model current disturbances in that area.

The principal cost of this flexibility is that only junctions and discontinuities having certain discrete sizes can be analyzed. For example, the width of the input or output port must be an integer multiple of W. In many cases this is not a problem, since interpolation can be used to determine the characteristics of a noninteger junction.

III. Results—Numerical and Experimental

The formulation described above was used to analyze a step discontinuity, a stub, and a bent stub. In this section, we compare the step discontinuity results predicted by this theory with the results predicted by Koster and Jansen. We then compare the stub results to measurements.

A. Step Discontinuity

In [7], Koster and Jansen presented the results of an analysis of the microstrip step discontinuity. The details of their formulation are not completely clear; however, they do refer to their method as having been described in a previous paper [4] on end effects. Some of the features of their analysis are that the expansion currents are entire domain in a local region near the discontinuity, the expansion currents approximate the edge condition, and the structure is enclosed in a conducting box. This is in contrast to the work presented here, which features finite element currents in an open or covered structure. These currents also approximate the edge condition, but do so with pulse and triangular functions. By not using currents which closely model the proper conditions at the edge, some accuracy is sacrificed; however, in many practical cases, this loss of accuracy is not significant. In return, a finite element approach allows the analysis of fairly complicated structures.

Using the finite element formulation, we have analyzed the step discontinuity for the substrate and frequency parameters used by Koster and Jansen. A comparison of the results shows that the S parameter magnitudes are almost identical and the phases show reasonable agreement. Fig. 2 shows a comparison of the phases calculated in this work to those calculated in [7]. The transmission phase is numerically a very stable result and differs from [7] by at most a couple of degrees. As reported in [7], the most sensitive quantity was found to be the S_{22} phase. For the results shown in Fig. 2, the size of the grid was six or ten sections in the transverse direction ($NM_y = 6$ or 10) and 28 in the longitudinal direction ($NM_x = 28$). The length of the total grid is slightly over π/β^-. More precisely, $L/2$ (defined in Fig. 1) is equal to $\pi/(\beta^-[NM_x - 2])$. Doubling NM_y has a negligible effect on the results. Increasing NM_x from 20 to 28 results in a change of slightly less than 1° for $W_2/W_1 = 3$ or 5 at $d/\lambda_0 = 0.04$. Our conclusion is that the S parameter magnitudes are very accurate and that the

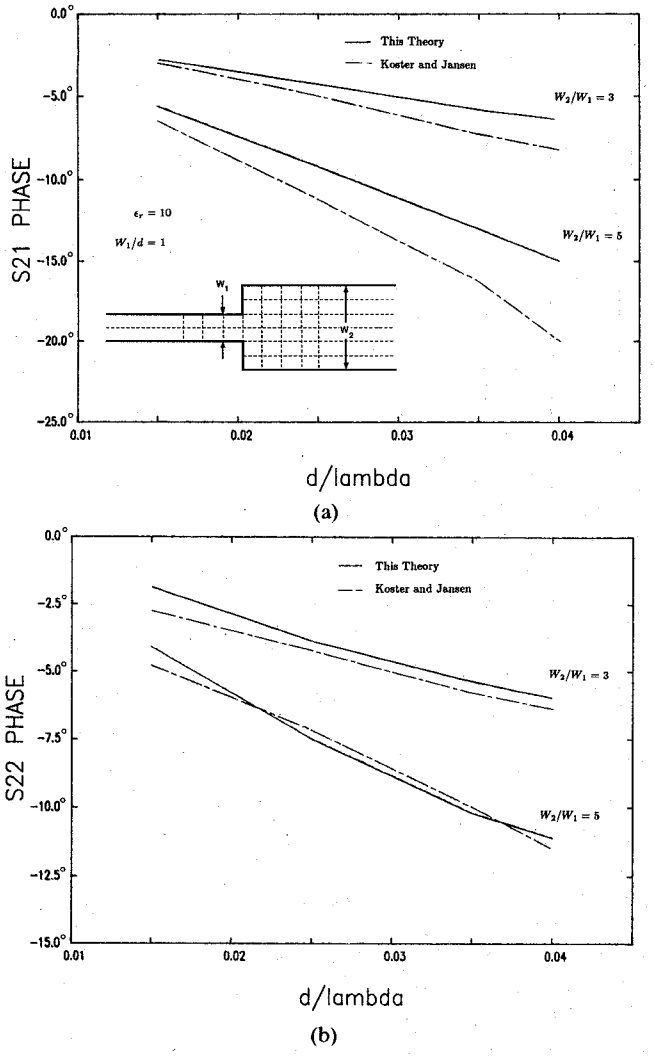

Fig. 2. Comparison of step phase calculations with those of Koster and Jansen [7]. (a) Transmission phase. (b) Reflection phase.

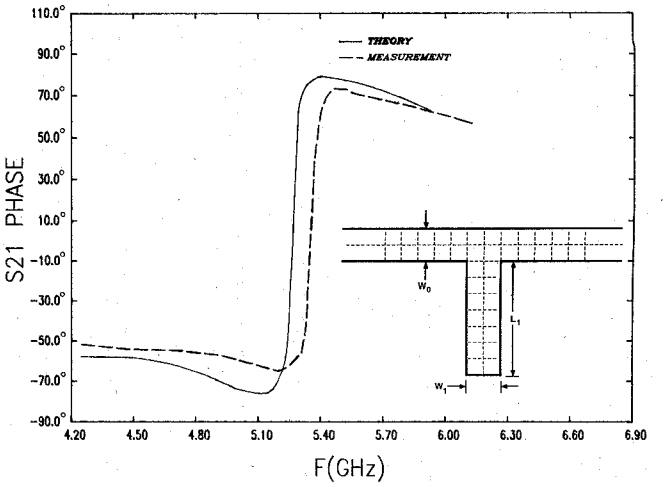

Fig. 3. Transmission phase of a single stub with measured (model) dimensions; $W_0 = 1.45$ mm (1.42), $W_1 = 1.40$ mm (1.40), $L_1 = 4.98$ mm (4.99).

phases are accurate to within one or two degrees. This is sufficient for most applications. For further accuracy, the currents at the edges must be modeled more carefully.

B. Stub

Fig. 3 shows the measured and calculated phase of a single open-circuit stub attached to a transmission line. Two discontinuities are evident: a tee junction and an open end. Note that the measured and calculated resonant frequencies (where the stub is one-quarter wavelength) differ by about 1.5 percent and the phase error is less than 7° over most of the band.

The stub structure was etched on the surface of a soft substrate (Duroid 6010.2) with a dielectric constant near 11 and a thickness of 1.27 mm. Stub dimensions were measured to within ± 0.025 mm. Transmission phase and magnitude were determined using a Hewlett Packard 8510 network analyzer. In order to reliably measure the phase, the following procedure was used. First, the connector–microstrip line–stub–microstrip line–connector phase was measured and the data stored. The stub was then carefully cut away and the assembly remeasured. By subtracting the phase of the second assembly from the phase of the first, we obtain the measured phase of the stub. This type of de-embedding technique is somewhat crude; however, it does not rely on the phase reproducibility of the connector transition or inhomogeneities in substrate permittivity. A reasonably good connector-to-microstrip transition is needed. In this case, each transition had a return loss of better than 25 dB. In order to accurately determine the substrate dielectric constant, the microstrip through line was further cut into several linear resonators [22]. The resonant frequency of each resonator was measured and used to determine that the dielectric constant was $\epsilon_r = 10.86 \pm 0.1$. The error is primarily due to errors in determining resonator dimensions (rough ends due to the cut).

The numerical model of the stub used nine divisions in the x direction and nine in the y. With reference to Fig. 1, both the dimensions $L/2$ and W are one-half the stub width. The input and output lines have the same width and are offset to the top of the grid. The model structure has slightly different dimensions from the actual measured structure, but these differences have an insignificant effect on resonant frequency. Due to the measurement uncertainties in the stub dimensions and in the dielectric constant (which are input to the analysis), the computed curve shown in Fig. 3 could be shifted by ± 1.5 percent in frequency from the nominal value shown. This would be a worst-case variation.

Note that a lossless ideal or quasi-static model for this junction predicts that the phase near resonance should jump from plus to minus 90°. The model presented here reproduces the measured *reduced* peak phase. This reduction may be due to radiation and conductor loss in the experiment and radiation loss in the model.

Figs. 4 and 5 illustrate some of the high-frequency characteristics which a full-wave analysis will reproduce. A shortened version of the stub shown in Fig. 3 was fabricated such that a resonance occurred near 10 GHz. This is a fairly high frequency for this substrate thickness and permittivity ($d/\lambda_0 = 0.04$, $d\sqrt{\epsilon_r}/\lambda_0 = 0.13$), and therefore

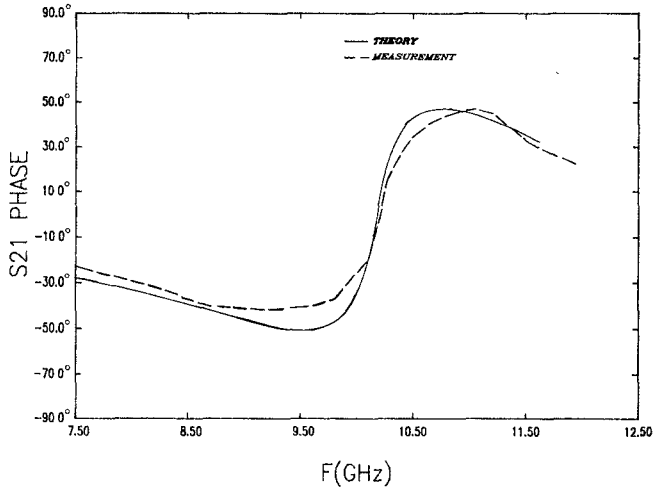

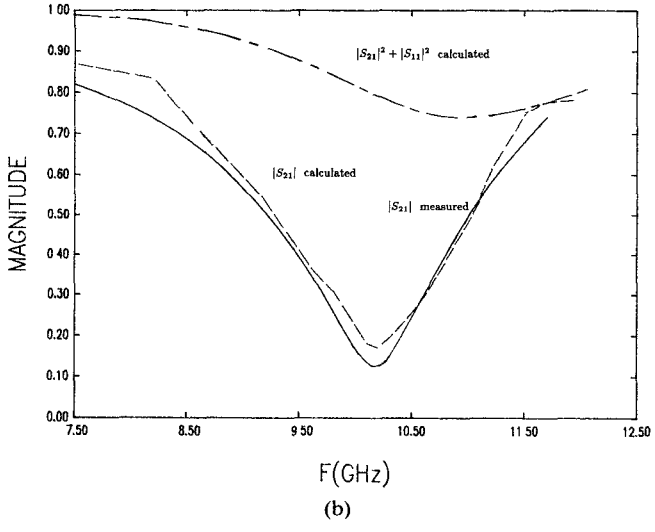

Fig. 4. Characteristics of a single stub with measured (model) dimensions; $W_0 = 1.40$ mm (1.45), $W_1 = 1.40$ mm (1.40), $L_1 = 2.16$ mm (2.17). (a) Transmission phase. (b) Transmission magnitude. $|S_{21}|^2 + |S_{11}|^2 < 1$ indicates radiation and surface wave loss.

significant coupling and radiation occur. To properly model the current in this case, the density of finite element modes was increased such that $L/2$ and W in Fig. 1 are one-quarter of a microstrip width (W_0).

Fig. 4 shows the measured and calculated transmission magnitude and phase. The measurements presented in Fig. 4 were performed in the manner described previously. Dielectric constant was determined to be 10.65 ± 0.15 and dimensional inaccuracies were as described previously. The uncertainty in these input quantities could cause a worst-case shift of the calculated curve by ± 1.5 percent. Agreement between measured and nominal calculation is excellent. Calculated peak phase is further reduced from the lower frequency case and measurements confirm this reduction. In addition, the calculated transmission isolation at resonance is reduced from roughly 40 dB (~ 35 dB measured) for the 5 GHz stub to 18 dB (15 dB measured) for the 10 GHz stub. A quasi-static calculation with or without loss does not show this reduced isolation.

Radiation loss can be an important effect for a substrate of this thickness. In Fig. 4b, we plot the quantity $G = |S_{21}|^2 + |S_{11}|^2$ based on the full-wave stub analysis. For a lossy junction, $(1 - G)$ is the fraction of incident power lost in the junction. The figure shows that the theoretical loss (to radiation and surface waves) peaks at about 25 percent near 11 GHz.

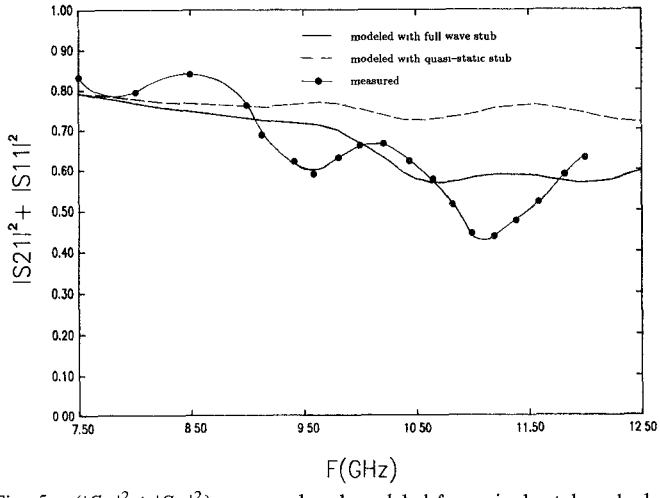

Fig. 5. $(|S_{21}|^2 + |S_{11}|^2)$ measured and modeled for a single stub embedded in the middle of a 5.1 cm transmission line (see text).

In order to verify the calculation, transmission and reflection measurements were made of a stub embedded between two microstrip lines, each 2.5 cm long. Fig. 5 plots the quantity G calculated from these measurements. No de-embedding was performed, and therefore the curve includes the conductor loss on the input and output lines. Measurements of the assembly with the stub cut off (a 5.0 cm through line) show a loss of 0.5 dB per inch. Incorporating this loss per unit length in a standard quasi-static model of the transmission line-stub-transmission line structure, results in a calculated G which is plotted in Fig. 5. This model includes conductor loss but not radiation loss. The stub length in the quasi-static model had to be adjusted so that the model resonant frequency coincided with the measured resonant frequency. Note that there is not a particularly good agreement with measurements above 9.0 GHz. Replacing only the quasi-static stub model with a two-port having the full-wave stub S parameters and leaving in the quasi-static lossy input/output lines results in the solid curve in the figure. This curve includes the conductor loss on the input and output lines and the radiation loss of the stub. Averaging the ripple in the measured curve (due to connector discontinuities) results in a curve which is in reasonable agreement with the full-wave stub model.

To summarize, the straight-stub full-wave analysis shows good agreement with measured data. Commercial CAD software using entirely quasi-static models shows good agreement in resonant frequency for the longer stub, but is high by about 7 percent for the shorter stub. Quasi-static models do not predict the measured reduction in peak phase variation unless conductor loss is included, and that will not account for the entire observed reduction.

The full-wave calculations in Fig. 4a include radiation and surface wave effects but not conductor loss. Since

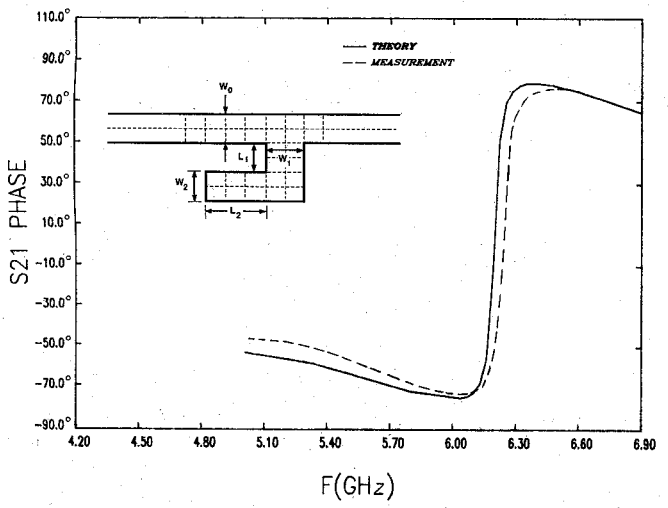

Fig. 6. Transmission phase of bent stub with measured (model) dimensions; $W_0 = 1.33$ mm (1.36), $W_1 = 1.35$ mm (1.39), $W_2 = 1.32$ mm (1.36), $L_1 = 1.38$ mm (1.36), $L_2 = 2.11$ mm (2.09).

there is good agreement with measurements, radiation and surface waves must play an important part, more so than conductor loss. Quasi-static models do not predict the reduced isolation measured at high resonant frequencies.

C. Bent Stub

Fig. 6 shows the measured and theoretical transmission phase of a bent stub. This is a very complex structure. It has three discontinuities: a tee, a 90° corner, and an open end. In addition, the stub is separated from the main line by one substrate thickness, and therefore coupling is a factor. As Fig. 4 shows, the agreement between measured and calculated results is excellent.

The measurement procedure and modeling parameters were similar to what was used on the low-frequency straight stub. A dielectric constant of 11.0 ± 0.1 was measured. The model dimensions were chosen such that the total length of the bent-stub model is the same as the total length of the measured stub. As a result of the discreteness which is inherent in the modeling procedure, the modeled widths (W_0, W_1, W_2) are slightly different from the actual widths in the measured structure. Measured and nominal calculated resonant frequency differ by 0.7 percent. Due to the uncertainty in the dielectric constant and the measured dimensions which are input to the analysis, the computed result could shift by ± 1.8 percent (worst case) in frequency.

A model of the same structure using quasi-static junction models and full-wave dispersive transmission lines gives a resonant frequency of 7.07 GHz—a 13 percent error. These results, plus the long straight-stub results (where the quasi-static model was good), indicate that coupling between different parts of the circuit is important.

It should be noted that coupling in this modeling scheme is not strong coupling (as in a Lange coupler). Strong coupling would require very accurate field calculations near interior edges.

IV. Conclusion

In this paper, we have presented a technique for analyzing irregular microstrip junctions. All electromagnetic effects, including radiation effects, are taken into account. No sidewalls are assumed, but a cover plate can easily be included if desired. Numerical results are stable to within one or two degrees of phase.

Measurements were made of three stub structures. Measured resonant frequencies agree with full-wave calculations to within 2 percent when nominal measured dielectric constant and structure dimensions were used as input. Using the absolute worst case dielectric constants and dimensions as input gives an error of 3 percent for the low-frequency stub and less than that for the other stubs. The measurements also show: (1) general agreement with calculated phase behavior to within 5–10°, (2) the effect of coupling within a structure, and (3) general agreement between calculated and measured radiation and surface wave loss.

A principal strength of this technique is its ability to model the effects of several discontinuities which are close enough to each other for coupling to occur.

Appendix I
Grounded Slab Green's Function

The tangential electric field components on the surface of a grounded dielectric slab are related to the tangential currents on the same surface via the following Green's function:

$$\vec{\vec{G}}(x, y, x_0, y_0) = \frac{1}{(2\pi)^2} \iint_{-\infty}^{\infty} dk_x\, dk_y\, \vec{\vec{Q}}(k_x, k_y)\, e^{jk_x(x-x_0)} e^{jk_y(y-y_0)} \quad \text{(A1)}$$

where

$$Q_{xx}(k_x, k_y) = -jZ_0 \sin(k_1 d) \cdot \frac{(\epsilon_r k_0^2 - k_x^2) k_2 \cos(k_1 d) + jk_1 (k_0^2 - k_x^2) \sin(k_1 d)}{k_0 T_e T_m} \quad \text{(A2)}$$

$$Q_{yx}(k_x, k_y) = jZ_0 k_x k_y \sin(k_1 d) \frac{k_2 \cos(k_1 d) + jk_1 \sin(k_1 d)}{k_0 T_e T_m} \quad \text{(A3)}$$

$$Q_{xy}(k_x, k_y) = Q_{yx}(k_x, k_y),\ Q_{yy}(k_x, k_y) = Q_{xx}(k_x \to k_y, k_y \to k_x)$$

where

$$\begin{aligned} k_2^2 &= k_0^2 - k_x^2 - k_y^2 \\ k_1^2 &= \epsilon_r k_0^2 - k_x^2 - k_y^2 \\ T_e &= k_1 \cos(k_1 d) + jk_2 \sin(k_1 d) \\ T_m &= \epsilon_r k_2 \cos(k_1 d) + jk_1 \sin(k_1 d). \end{aligned} \quad \text{(A4)}$$

APPENDIX II
INFINITE MICROSTRIP LINE

In this appendix, we present the formulation used to precompute the propagation constant β and the transverse dependency of the x- and y-directed currents on the input and output lines. The procedure is standard, but is outlined here in order to show how it fits in with the discontinuity calculation.

Assuming a current distribution of the form

$$\vec{J}(x, y) = e^{-jhx}\left[g_{xs}(y)\hat{x} + jg_{ys}(y)\hat{y}\right] \tag{A5}$$

(1) gives the following expression for $\vec{E}$:

$$\vec{E}_i = \frac{e^{-jhx}}{2\pi}\int_{-\infty}^{\infty} dk_y\left[Q_{ix}(-h, k_y)G_{xs}(k_y) + jQ_{iy}(-h, k_y)G_{ys}(k_y)\right]e^{jk_y y} \tag{A6}$$

where $i = x$ or y and G_{xs}, G_{ys} are the Fourier transforms of g_{xs}, g_{ys}.

The functions g_{xs} and g_{ys} are now expanded so that

$$g_{xs}(y) = \sum_{m=1}^{N_y} c_m g_x^m(y) \tag{A7a}$$

$$g_{ys}(y) = \sum_{m=1}^{N_y-1} d_m g_y^m(y) \tag{A7b}$$

where

$$g_x^m(y) = s(y/W - [m-1/2]) + s(y/W + [m-1/2]) \tag{A8a}$$

$$g_y^m(y) = t(y/2W - m/2) - t(y/2W + m/2) \tag{A8b}$$

and the functions s and t were defined in (6). N_y and W are chosen such that the total width of the microstrip line is $2N_yW$. Equations (A7) are then Fourier transformed and combined with (A6). Following the well-known moment method procedure, functions (A8) are used to test that the electric field generated by (A6) is zero on the conductor surface. The resulting impedance matrix is

$$\begin{bmatrix} \vec{\vec{Z}}_{xx}^{\infty}(h) & \vec{\vec{Z}}_{xy}^{\infty}(h) \\ \vec{\vec{Z}}_{yx}^{\infty}(h) & \vec{\vec{Z}}_{yy}^{\infty}(h) \end{bmatrix} \begin{bmatrix} c_1 \\ \vdots \\ c_{N_y} \\ d_1 \\ \vdots \\ d_{N_y-1} \end{bmatrix} = \begin{bmatrix} \vdots \\ 0 \\ \vdots \end{bmatrix} \tag{A9}$$

where

$$\left(Z_{xx}^{\infty}\right)_{m,n} = \frac{1}{2\pi}\int_{-\infty}^{\infty} dk_y G_x^{m*}(k_y)Q_{xx}(-h, k_y)G_x^n(k_y) \tag{A10a}$$

$$\left(Z_{xy}^{\infty}\right)_{m,n} = \frac{1}{2\pi}\int_{-\infty}^{\infty} dk_y G_x^{m*}(k_y)Q_{xy}(-h, k_y)jG_y^n(k_y) \tag{A10b}$$

$$\left(Z_{yy}^{\infty}\right)_{m,n} = \frac{1}{2\pi}\int_{-\infty}^{\infty} dk_y G_y^{m*}(k_y)Q_{yy}(-h, k_y)G_y^n(k_y). \tag{A10c}$$

The value of h which makes the determinant of Z^{∞} zero is the propagation constant β. The values of c_i, d_j can then be determined from (A9) and combined with (A7) to generate $g_{xs}(y)$ and $g_{ys}(y)$. The coefficients $\{c_i, d_i\}$ and β are stored for use in the discontinuity calculation.

ACKNOWLEDGMENT

The author wishes to express his thanks to J. J. Burke for his very careful measurements.

REFERENCES

[1] P. Silvester and P. Benedek, "Microstrip discontinuity capacitances for right-angle bends, T-junctions and crossings," *IEEE Trans. Microwave Theory Tech.*, vol. MTT-21, pp. 341–346, 1973.

[2] A. Gopinath *et al.*, "Equivalent circuit parameters on microstrip step change in width and cross junctions," *IEEE Trans. Microwave Theory Tech.*, vol. MTT-24, pp. 142–144, 1976

[3] R. H. Jansen, "Hybrid mode analysis of end effects of planar microwave and millimeter wave transmission lines," *Proc. Inst. Elec. Eng.*, vol. 128, pt. H, pp. 77–86, Apr. 1978.

[4] J. Boukamp and R. H. Jansen, "The high frequency behavior of microstrip open ends in microwave integrated circuits including energy leakage," in *Proc. 14th European Microwave Conf.*, 1984, pp. 142–147.

[5] R. W. Jackson and D. M. Pozar, "Microstrip open-end and gap discontinuities," *IEEE Trans. Microwave Theory Tech* , vol. MTT-33, pp. 1036–1042, Oct. 1985.

[6] P. B. Katehi and N. C. Alexopoulos, "Frequency-dependent characteristics of microstrip discontinuities in millimeter-wave integrated circuits," *IEEE Trans. Microwave Theory Tech.*, vol. MTT-33, pp. 1029–1035, Oct. 1985.

[7] N. H. L. Koster and R. H. Jansen, "The microstrip step discontinuity: A revised description," *IEEE Trans. Microwave Theory Tech.*, vol. MTT-34, pp. 213–223, Feb. 1986.

[8] R. Sorrentino and T. Itoh, "Transverse resonance analysis of finline discontinuities," *IEEE Trans. Microwave Theory Tech.*, vol. MTT-32, pp. 1633–1638, Dec. 1984.

[9] H. El-Hennawy and K. Schunemann, "Impedance transformation in fin lines," *Proc. Inst. Elec. Eng.*, vol. 129, pp. 342–350, Dec. 1982.

[10] K. C. Gupta *et al.*, *Computer-Aided Design of Microwave Circuits*. Dedham, MA: Artech House, 1981.

[11] T. Okoshi, *Planar Circuts for Microwaves and Lightwaves*. New York: Springer Verlag, 1985.

[12] G. Kompa, "S-matrix computation of microstrip discontinuities and a planar waveguide model," *Arch. Elek. Übertragung.*, vol. 30, pp. 58–64, 1976.

[13] R. H. Jansen, "High-order finite element polynomials in the computer analysis of arbitrarily shaped microstrip resonators," *Arch. Elek. Übertragung.*, vol. 29, pp. 241–247, 1975.

[14] J. R. Mosig and F E. Gardiol, "General integral equation formulation for microstrip antennas and scatterers," *Proc. Inst. Elec. Eng.*, vol. 132, pt. H, no. 7, pp. 425–432, Dec. 1985.

[15] J. R. Mosig, "Arbitrarily shaped microstrip structures and their analysis with a mixed potential integral equation," *IEEE Trans. Microwave Theory Tech.*, vol. 36, pp. 314–323, Feb. 1988.

[16] S. B. Worm and R. Pregla, "Hybrid-mode analysis of arbitrarily shaped planar microwave structures by the method of lines," *IEEE Trans. Microwave Theory Tech.*, vol. MTT-32, pp. 186–191, Feb. 1984.

[17] J. C. Rautio and R. F. Harrington, "An electromagnetic time-harmonic analysis of shielded microstrip circuits," *IEEE Trans. Microwave Theory Tech.*, vol. MTT-35, pp. 726–730, Aug. 1987.

[18] R. H. Jansen, "Modular source-type 3D analysis of scattering parameters for general discontinuities, components and coupling effects in (M)MICs," in *17th European Microwave Conf. Proc.*, (Rome, Italy), 1987, pp. 427–432.

[19] R. W. Jackson, "Considerations in the use of coplanar waveguide for millimeter-wave integrated circuits," *IEEE Trans. Microwave Theory Tech.*, vol. MTT-34, pp. 1450–1456, Dec. 1986.

[20] R. H. Jansen, "The spectral domain approach for microwave integrated circuits," *IEEE Trans. Microwave Theory Tech.*, vol. MTT-33, pp. 1043–1056, 1985.
[21] D. M. Pozar, "Input impedance and mutual coupling of rectangular microstrip antennas," *IEEE Trans. Antennas Propagat.*, vol. AP-30, pp. 1191–1196, Nov. 1982.
[22] T. C. Edwards, *Foundations for Microstrip Circuit Design*. New York: Wiley, 1981, p. 189.

✠

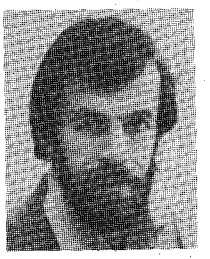

Robert W. Jackson (M'82–SM'88) was born in Boston, MA, on October 18, 1952. He received the B.S. (1975) and Ph.D. (1981) degrees in electrical engineering from Northeastern University, Boston, MA. His thesis was on nonlinear plasma interactions in the earth's bow shock.

From 1981 to 1982 he was an Assistant Professor at Northeastern University. Since 1982, he has been on the faculty of the Department of Electrical and Computer Engineering at the University of Massachusetts, Amherst, where he is a member of the Microwave and Electronics Laboratory. His research interests include numerical electromagnetics applied to millimeter-wave integrated circuits and active microwave and millimeter-wave circuit design.